



RESEARCH ARTICLE

OCTOPOD: single-bunch tomography for angular-spectral characterization of laser-driven protons

M. Reimold^{1,2,5}, S. Assenbaum^{1,2}, E. Beyreuther^{1,3}, E. Bodenstern³, F.-E. Brack¹, C. Eisenmann¹, F. Englbrecht⁴, F. Kroll¹, F. Lindner⁴, U. Masood¹, J. Pawelke^{1,3}, U. Schramm^{1,2}, M. Schneider^{1,2,3}, M. Sobiella¹, M. E. P. Umlandt^{1,2}, M. Vescovi^{1,2}, K. Zeil¹, T. Ziegler^{1,2}, and J. Metzkes-Ng¹

¹Helmholtz-Zentrum Dresden – Rossendorf, Dresden, Germany

²Technische Universität Dresden, Dresden, Germany

³Oncoray – National Center for Radiation Research in Oncology, Dresden, Germany

⁴Ludwig-Maximilians-Universität München, Garching/ München, Germany

⁵Currently at: Universitätsklinikum Freiburg, Freiburg, Germany

(Received 31 March 2023; revised 31 May 2023; accepted 28 June 2023)

Abstract

Laser–plasma accelerated (LPA) proton bunches are now applied for research fields ranging from ultra-high-dose-rate radiobiology to material science. Yet, the capabilities to characterize the spectrally and angularly broad LPA bunches lag behind the rapidly evolving applications. The OCTOPOD translates the angularly resolved spectral characterization of LPA proton bunches into the spatially resolved detection of the volumetric dose distribution deposited in a liquid scintillator. Up to 24 multi-pinhole arrays record projections of the scintillation light distribution and allow for tomographic reconstruction of the volumetric dose deposition pattern, from which proton spectra may be retrieved. Applying the OCTOPOD at a cyclotron, we show the reliable retrieval of various spatial dose deposition patterns and detector sensitivity over a broad dose range. Moreover, the OCTOPOD was installed at an LPA proton source, providing real-time data on proton acceleration performance and attesting the system optimal performance in the harsh laser–plasma environment.

Keywords: laser–plasma acceleration of protons; proton detector; tomographic reconstruction

1. Introduction

Laser-driven solid density plasmas – generated in the interaction of a focused high-power laser pulse with the surface of a μm to nm thin foil – can sustain electric field strengths of TV/m. These fields enable compact and efficient particle acceleration, generating proton bunches exceeding 80 MeV kinetic energy on μm spatial scales^[1]. The intense proton bunches with only ps bunch duration at the source feature unprecedented dose rates exceeding 10^9 Gy/s, and hence make laser–plasma acceleration a unique laboratory-scale tool for the currently intensively studied field of ultra-high-dose-rate radiobiology^[2].

While applications in radiobiology^[3] and material characterization are rapidly developing^[4], the complete characterization of the primary proton bunches as emitted from the laser–plasma accelerated (LPA) source still poses a major instrumental challenge. The proton emission occurs from an approximately $100\ \mu\text{m}$ source area (see Ref. [5] and references therein) into a large energy-dependent cone of $200\text{--}400$ mrad^[6] half-opening angle and an exponentially decreasing energy spectrum up to a cut-off energy. Established direct spectral detection methods such as Thomson parabola^[7–10] or time-of-flight spectrometers^[11–14] only resolve the energy spectrum for a small solid angle of the full distribution. To capture the full solid angle, the spectral measurement is performed by absorbing the proton bunch in a detector volume, yielding the corresponding spatially resolved 3D dose distribution from which the energy spectrum is deconvoluted. Dose-based spectral characterization

Correspondence to: J. Metzkes-Ng, Helmholtz-Zentrum Dresden – Rossendorf, 01328 Dresden, Germany. Email: j.metzkes-ng@hzdr.de

has been implemented with several detector types from stacks of radiochromic film (RCF)^[10,15] to scintillators^[16–24] and ultrasound-based methods^[25,26], yielding the angularly resolved spectrum with different granularity in either angle and/or energy. However, only scintillator- and ultrasound-based approaches in principle allow for real-time readouts. Yet, as implemented so far, the according detectors feature an angular and spectral resolution that is reduced in comparison to RCF.

The instrumental limits of current techniques regarding angular and spectral resolution as well as real-time operation are improved with the OCTOPOD detector, short for Optical Cone beam TOMograph for Proton Online Dosimetry. In the OCTOPOD detector, a proton bunch is absorbed in a cylindrical liquid scintillator volume of 5 cm diameter and 4.3 cm water-equivalent path length (for a scintillator density of 0.86 g/cm³^[27]), sufficient to stop protons up to 70 MeV kinetic energy. 2D projections of the 3D photon emission distribution are recorded via pinhole imaging onto 2D optical sensors for multiple angles, allowing for a tomographic image reconstruction of the 3D photon emission, as in single photon emission computed tomography (SPECT) medical imaging^[28]. Retrieval of the angularly resolved energy spectrum then in principle requires spectral deconvolution as established for RCF measurements^[29] after tomographic reconstruction of the 3D light emission pattern and signal calibration to dose.

In this paper, we present the detector setup and its characterization at a cyclotron proton source. Finally, the

OCTOPOD is implemented at the Draco PW^[30,31] LPA proton source at Helmholtz-Zentrum Dresden–Rossendorf (HZDR) and provides for the first time real-time data of the complete accelerated proton bunch.

2. Detector design and signal reconstruction algorithms

2.1. Detector setup

The central detection element of the OCTOPOD (Figure 1) is a volume of liquid scintillator (Saint-Gobain, BC-517H, 425 nm, $n_{\text{ref}} = 1.476$) of 5 cm diameter and length. Using a liquid scintillator prevents localized radiation damage and allows for a regular material exchange in the case of severe radiation damage. Light emission of the scintillator is in the visible range (maximum of emission at 425 nm) and can hence be detected with standard silicon-based sensors.

The scintillator volume is housed in an octagonal polymethylmethacrylate (PMMA) block with a 5 cm wide base and the length of 7 cm, and the proton bunch enters through a 1 mm thick PMMA plate (Figures 1(b) and 1(c)). The PMMA block guides light emitted in the scintillator volume to the optical sensors. The nearly identical refractive indices of the scintillator material and PMMA ($n_{\text{ref}} = 1.49$) in combination with the perfect surface connection of the liquid and solid material keep the light transport from the scintillator volume to the light detection system refraction-free. This minimizes the overall detector size to a compact diameter of 23 cm and length of 10 cm.

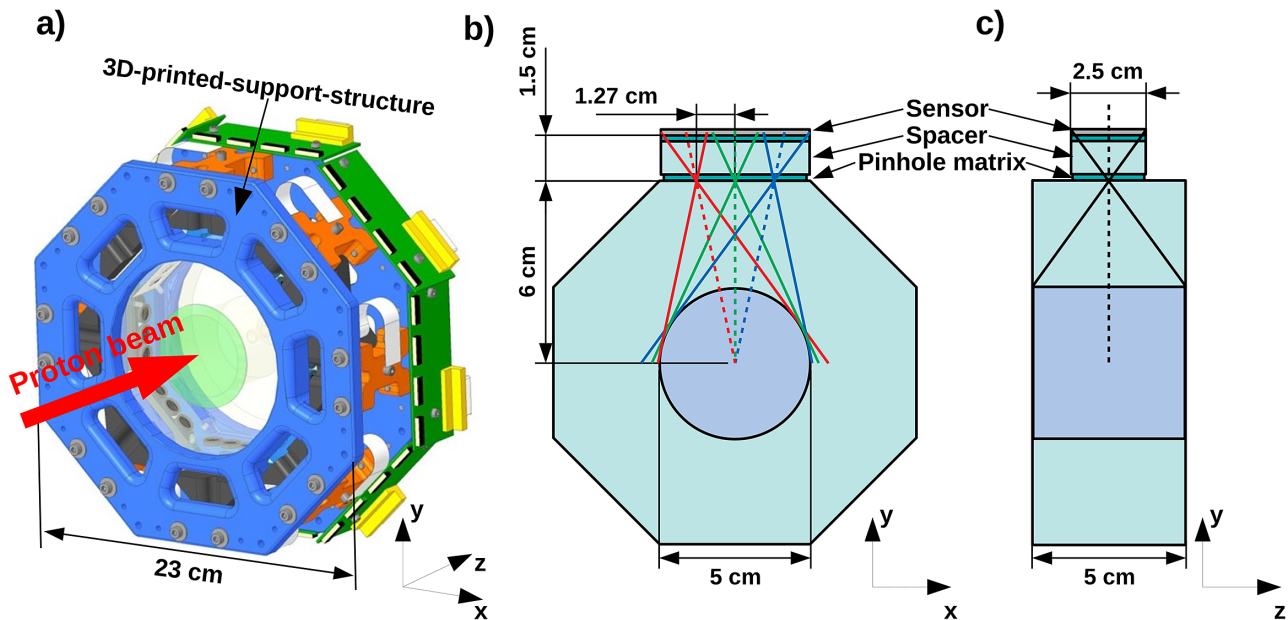


Figure 1. The design of the OCTOPOD (Optical Cone beam TOMograph for Proton Online Dosimetry) detector. (a) 3D view of the octagonally shaped OCTOPOD detector with an outer diameter of 23 cm. (b) The schematic frontal cut-plane of the OCTOPOD with the 5 cm diameter reconstruction volume filled with liquid scintillator (in blue), the octagonal polymethylmethacrylate (PMMA) housing (in green) enclosing the reconstruction volume and connecting to the three pinholes and the sensor plane at the distance of 1.5 cm defined by a PMMA cuboid. The setup is repeated for each side of the octagonal PMMA housing to obtain 24 cone beam (CB) projections of the reconstruction volume. (c) The schematic side cut-plane with the 5 cm long reconstruction volume.

The imaging system uses a pinhole camera concept to generate cone beam (CB) projections of the reconstruction volume (Figures 1(b) and 1(c)). The CB imaging is realized using pinholes that restrict the light transmission of the side surfaces of the PMMA octagon to circular 200 μm diameter spots. This enables imaging with a resolution of 1 mm in the center of the reconstruction volume for the applied image plane distance of 1.5 cm behind the pinholes:

$$R = d \cdot \left(1 + \frac{1}{M}\right) = 200 \mu\text{m} \times \left(1 + \frac{6 \text{ cm}}{1.5 \text{ cm}}\right) = 1 \text{ mm}. \quad (1)$$

Here, d is the pinhole diameter, M is the magnification and R is the resolution. For each side of the PMMA octagon, a three-pinhole geometry is used, with a pinhole centered with respect to the reconstruction volume (green cone in Figure 1(b)) and two other pinholes (red/blue cones in Figure 1(b)) that are laterally shifted by ± 1.27 cm. This geometry allows one to obtain three CB projections of the reconstruction volume with one 2D pixelated RadEye remote sensor (Rad-Icon, 2.46 cm \times 4.92 cm sensitive area, 48 μm pixel pitch). This sensor type provides a large sensitive area and can be read-out via remote electronics, which minimizes the detector size at the position of readout. RadEye detectors have been applied widely as particle and light detectors for LPA sources^[32–34].

The sensors are attached to the octagon surface via 1.5 cm thick cuboid PMMA spacers fitting the size of the sensor sensitive area and defining the image plane distance from the pinholes (Figures 1(b) and 1(c)). The boundary connections among the PMMA octagon, pinholes, PMMA spacer and sensor are optimized for light transport with the help of silicone grease (Saint-Gobain, BC-630, $n_{\text{ref}} = 1.465$). With the octagonal symmetry of the detector design, eight sensors are used to obtain 24 CB projections of the reconstruction volume.

2.2. Detector response matrix

The tomographic signal reconstruction from the measured CB projections is performed via an iterative maximum likelihood expectation maximization (MLEM) algorithm. The MLEM algorithm iteratively compares measured and estimated CB projections to predict the most likely 3D scintillation light distribution in the reconstruction volume. An essential part of the MLEM algorithm is hence the forward projection, where the voxel signal values in the reconstruction volume are projected onto the sensor pixels to obtain a CB projection image that can be compared with the measured data. In the reverse, that is, the back-projection, the sensor pixel values are projected into the reconstruction volume voxels to obtain the 3D scintillation light signal.

Those forward and backward projections are defined by the fixed OCTOPOD setup and are generated via a ray tracing

algorithm performed prior to the reconstruction. The respective algorithm calculates the relative signal contribution of each voxel in the reconstruction volume to the projected value on a certain pixel of the sensor and stores the result in a look-up table. To reduce the size of the look-up table, the sensor pixels are binned by a factor of 4 such that the pixel matrix of 512 \times 1024 reduces to 128 \times 256 and the pixel pitch increases from 48 to 192 μm . This step does not affect the 1 mm spatial resolution in the center of the reconstruction volume for the 200 μm diameter pinhole, because the magnification of $M = 0.25$ yields a signal resolution on the sensor area of 250 μm . In addition, making use of the two symmetry axes of the setup's geometry for one sensor allows for a further reduction of the pixel number that must be investigated by the ray tracing algorithm by a factor of 4.

The ray tracing algorithm samples random coordinates on the sensor pixel surfaces and the corresponding pinhole area (the geometry prohibits one pixel from seeing a signal from two different pinholes) and calculates 1000 lines defined by these two coordinates. For each voxel that is intersected by a calculated line, the length of the straight in the voxel is calculated and assigned to the voxel. If a voxel is intersected multiple times, the intersection lengths are summed up and divided by the number of intersections. Voxels that are not intersected have the value of zero. To account for the inverse-square law, each voxel value is also weighted by $1/r_1^2$, where r_1 is the distance between the voxel and the pinhole. Equivalently, all intersected voxels for a single pixel are weighted with the factor $1/r_2^2$, where r_2 is the distance between the pinhole and the sensor pixel. The thickness of the pinhole of 100 μm leads to an angle-dependent effective pinhole area, which is considered by the ray tracing algorithm by weighting all the intersected voxels for a certain sensor pixel with the corresponding effective pinhole area and restricting the random coordinate sampling to the effective pinhole area.

Back-projection for each sensor of a homogeneous image with pixel values equal to 1 into the reconstruction volume yields the relative sampling efficiency for each voxel. The relative sampling efficiency for each voxel is determined by its position within the reconstruction volume and determined by the distance to the pinholes via the inverse-square law and the effective pinhole size, as described above. The inverse of the back-projected result forms the matrix used in the MLEM algorithm to correct for the sampling efficiency (Figure 2).

2.3. Multi-pinhole grids

The signal readout from the reconstruction volume with single 200 μm diameter pinholes strongly limits the sensitivity of the detector and yields a high threshold dose for detection. Increasing the detector sensitivity by using larger pinholes is efficient as the signal increases quadratically with the pinhole diameter, but comes at the cost of

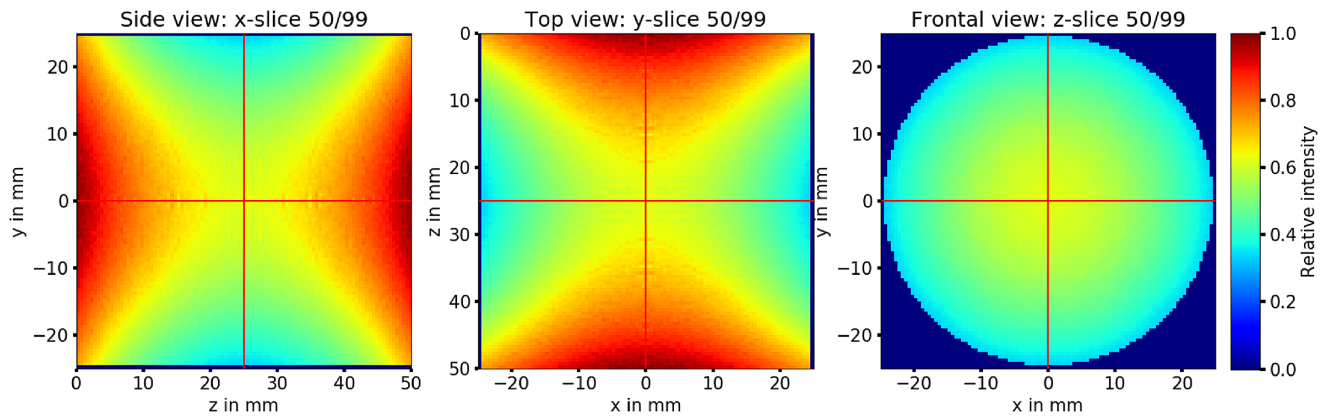


Figure 2. The correction matrix for the reconstruction algorithm showing the inverse relative sampling efficiency for all voxels in the reconstruction volume. From left to right, the side cut-plane, the top cut-plane and the frontal cut-plane of the 3D distribution are shown. For the side and top view, maximum correction is required for the front and rear part of the reconstruction volume ($z \approx 0$ mm, $z \approx 50$ mm) where the distance to the pinholes is maximized and the effective pinhole size is minimized. For the frontal view taken at the center of the reconstruction volume, the detection efficiency is solely determined by the inverse-square law effect because the effective pinhole size does not change. Hence, the required signal correction increases towards the reconstruction volume center.

reducing the spatial resolution (Equation (1)). This problem is circumvented by using grids of multiple small pinholes (multi-pinhole grids), which increase the sensor signal by spatially overlapping CB projections then integrated by the sensor. This technique is often used in SPECT^[28]. The reconstruction of the single-pinhole CB projection from the obtained multi-pinhole projections is performed with an iterative Richardson–Lucy deconvolution algorithm^[35]. This iterative algorithm allows one to reconstruct an original image measured with an optical system that can be described with a line spread function (LSF), as for example, the multi-pinhole grids here.

3. OCTOPOD characterization at a proton cyclotron

3.1. Experimental setup

First measurements with the OCTOPOD were performed at University Proton Therapy Dresden (UPTD; Dresden, Germany), which operates an isochronous cyclotron (Cyclone 230, Proteus Plus clinical facility, IBA) with an experimental hall equipped with a horizontal fixed-beam proton beamline^[36] (Figure 3(a)). The goal was to investigate the MLEM reconstruction algorithm, to test the detector sensitivity and to benchmark the multi-pinhole reconstruction algorithm based on experimental data. The proton beamline was operated at output energies between 70 and approximately 90 MeV, generating Bragg peak (BP) depth dose profiles in the detector volume. A range compensator (2 cm thick PMMA block) was placed in front of the detector entrance window to shift the BP position into the sensitive volume of the detector (Figure 3(b)). In addition, the measurement of a 70 MeV proton BP was performed with a half-blocked beam (Figure 3(c)). The lateral proton beam profile had a

size of 20 mm, provided by the beamline without additional scatterers in place.

The OCTOPOD was set up in two configurations. First, two out of eight possible sensors were installed, each sensor equipped with a different pinhole geometry (single pinhole 200 μm diameter, 3×3 pinhole grid 200 μm diameter). To yield sufficient projections of the sensitive volume, the OCTOPOD detector was rotated eight times about the proton beam axis in steps of 45° . Second, all eight sensors were equipped with 91-pinhole grids, to further increase the detector sensitivity.

3.2. Reconstruction of the 3D signal

Exemplary reconstructed BP data recorded with the single pinhole with and without the range shifter in place as well as with the half-blocked proton beam are shown in Figure 3. The relative signal intensity is proportional to the scintillator light output. The effect of the range shifter is clearly visible and the half-blocked beam setup generates a clear signal edge in the side cut-plane. Both features show that the detector concept and signal reconstruction are viable for the purpose of resolving 3D dose distributions.

To investigate the number of iterations required to reconstruct a BP with the MLEM algorithm, the depth dose profile of the reconstructed signal is monitored for each iteration step (Figure 4). The depth profile of the signal is generated by summing up the reconstructed 3D dose signal along both lateral dimensions. The reconstructed signal converges well within 20 iteration steps, with two features being visible. Firstly, there is a signal decrease in the detector's entrance region, which is attributed to integrated background remaining from the CB back-projections into the reconstruction volume. Secondly, comparing the MLEM

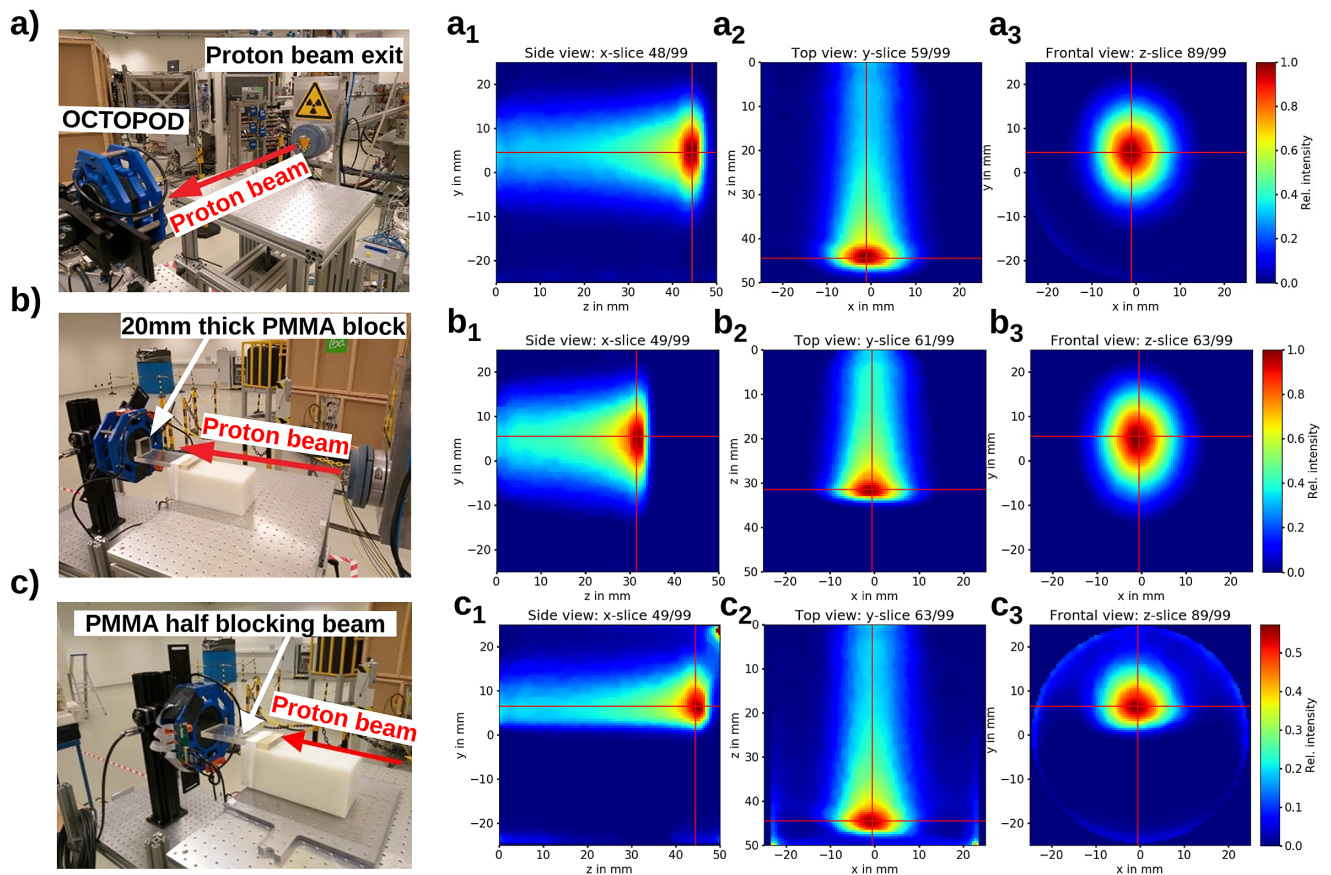


Figure 3. The single-pinhole measurements performed at the experimental proton beamline at University Proton Therapy Dresden (UPTD) with one sensor installed and a rotating detector for three different proton beam setups. The reconstructed 3D signals are shown as the side cut-plane (a_1)–(c_1), the top cut-plane (a_2)–(c_2) and the frontal cut-plane (a_3)–(c_3). The red lines in each view mark the position of the other cut-planes with respect to the presented view. (a) Experimental setup and reconstruction of the 70 MeV Bragg peak (BP). (b) Experimental setup and reconstruction of the 80 MeV BP with a 2 cm polymethylmethacrylate (PMMA) block in front of the detector. (c) Experimental setup and reconstruction of the 70 MeV BP with a PMMA block half-blocking the proton beam in front of the detector. Note that here the maximum of the colorbar of the reconstruction was adjusted to the maximum signal in the BP since scattered protons directly detected by the upper sensor positions lead to an artefact in the reconstruction visible in the upper right corner of the side cut-plane.

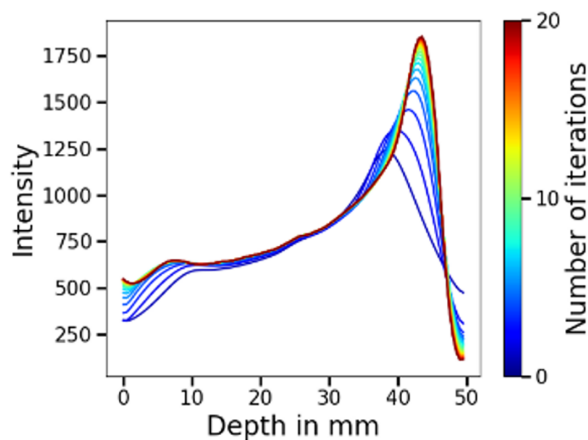


Figure 4. The iteration steps of the reconstruction algorithm shown as the laterally integrated 3D reconstruction signal plotted over the penetration depth for the 70 MeV Bragg peak (BP) reconstruction.

algorithm performance for BPs stopping towards the edge versus in the middle of the reconstruction volume, the latter show a faster convergence. The efficiency of the construction algorithm is optimal where the projection lines through the reconstruction volume are orthogonal to the beam axis (i.e., middle of the reconstruction volume) and is reduced where the projection lines traverse the reconstruction volume at a shallow angle.

3.3. Detector sensitivity with multi-pinhole grids

To increase the sensitivity of the OCTOPOD detector, multi-pinhole grids with 3×3 pinholes and 91 pinholes as an alternative to imaging via a single pinhole were tested. **Figure 5** compares all three pinhole options regarding geometry, LSF and measured/deconvoluted image. The summary

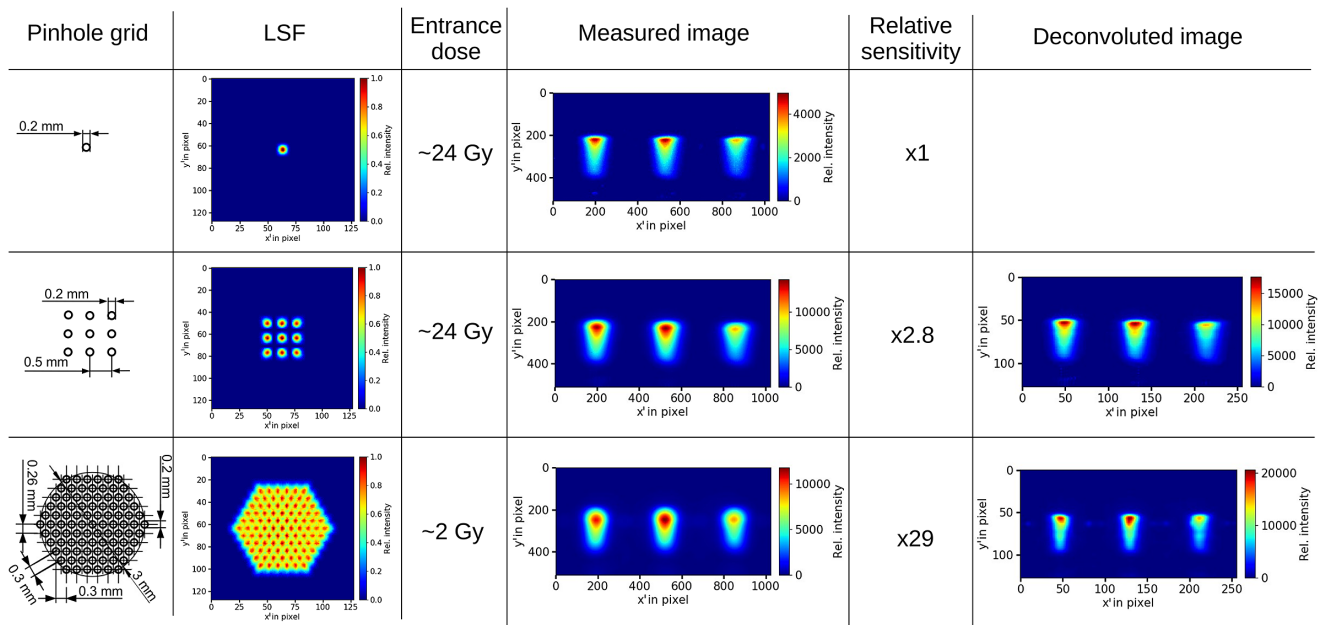


Figure 5. The deconvolution of the measured cone beam (CB) projections compared for single-pinhole and multi-pinhole geometries for an 80 MeV proton Bragg peak (BP, 2 cm polymethylmethacrylate (PMMA) in front of the detector). Increasing the number of pinholes leads to a higher sensitivity but also changes the shape of the obtained projections. The original shape of the CB projections is reconstructed in a deconvolution with the line spread functions (LSFs) of the pinhole geometry using an iterative Richardson–Lucy deconvolution algorithm^[35].

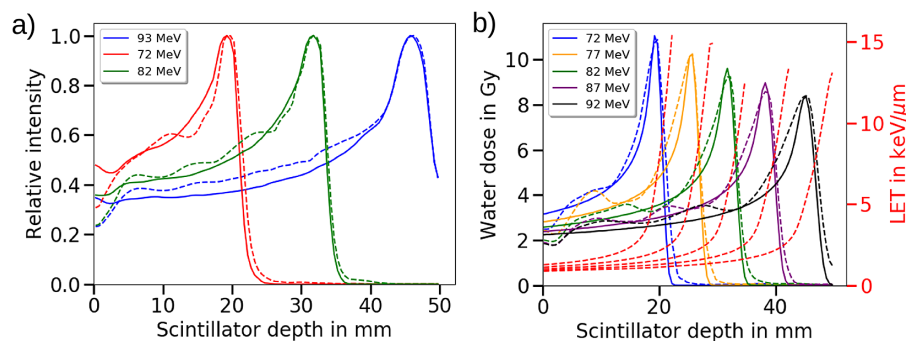


Figure 6. Comparison of the reconstruction performance for different single pinholes and multi-pinhole grids. (a) The performance comparison between the 1D depth signal profiles of Bragg peaks (BPs) measured with a single pinhole (solid lines) and a 3×3 pinhole grid (dashed lines). The data were simultaneously measured with two different sensors (one sensor with single-pinhole geometry and the other with a 3×3 pinhole grid) and a rotating detector. (b) The 1D depth signal profiles for a 91-pinhole grid, applied for all eight sensors simultaneously. The measured profiles (solid lines, corrected for LET quenching) are compared to simulated (dashed lines) depth dose profiles obtained in a lateral 5 mm diameter region centered in the BP. Note that the BPs are labeled with an offset of +2 MeV, which needs to be introduced in the Monte Carlo (MC) simulation to benchmark the measured depth dose profiles against RCF measurements.

shows that the entrance dose required to measure reasonable data reduces from the level of 24 Gy in the case of the single pinhole by a factor of 3 for the 3×3 pinhole grid to the level of approximately 1 Gy for the 91-pinhole grid. This sensitivity level fits the requirements of LPA proton sources. The increase in sensitivity comes at the cost of a smearing of the signal, as visible in the decreasing sharpness of the BPs' distal edges (position $y = 200$ px) in the measured images with increasing pinhole numbers. This effect is however corrected for in the unfolding, as visible in the according deconvoluted images. In the following, the performance of the multi-pinhole unfolding and reconstruction of the 3D signal will be discussed in detail.

Data for reconstructed depth dose profiles of BPs for proton energies of 70, 80, 91 MeV with the range shifter in place are compared for the single pinhole and the 3×3 pinhole grid (Figure 6(a)). Both pinhole configurations show a perfect agreement in proton range in the sensitive volume. Minor artifacts introduced by the multi-pinhole grid are some wave-like patterns in the plateau region of the BP and a slightly higher plateau region. In addition, the entrance signal is reduced compared to the single pinhole, an effect most likely originating from the less efficient overlapping of the single CB projections in the detector's entrance region.

To further increase the sensitivity of the OCTOPOD, the reconstruction performance of the hexagonal grid with

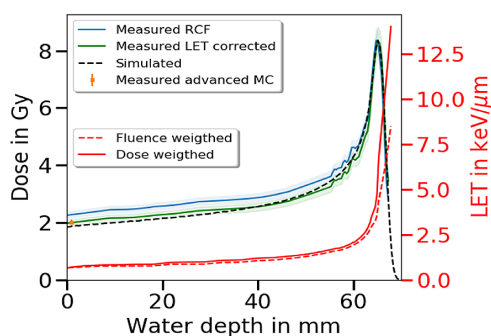


Figure 7. Comparison of Monte Carlo (MC) simulation results (dashed lines) with the 3D dose distribution measured with a calibrated stack of radiochromic films (RCFs, type EBT3 from Gafchromic, solid lines). The depth dose distributions shown are derived from the volumetric dose measurement by averaging over a lateral 5 mm diameter region centered on the proton beam profile. The dose- and fluence-weighted depth-dependent distributions of the linear energy transfer (LET) are derived from the MC simulations and are used to correct the RCF response according to Ref. [37]. The dose in the plateau region was additionally measured with an Advanced Markus ionization chamber (AMC, type 34045, PTW). Since the calibration of the RCFs was performed in the middle of a spread-out Bragg peak, the calibration LET is closer to the LET at the BP maximum than to the lower LET at the entrance plateau. Therefore, the maximum of the LET-corrected RCF dose distribution is normalized to the maximum of the dose distribution measured with the RCF stack, leading to an agreement with the entrance dose measured with the AMC and the simulated depth dose profile.

91 pinholes is investigated, now with all eight sensors in operation to allow for single beam measurements without moving the detector setup. Reconstructed depth dose profiles for proton energies of 70, 75, 80, 85, 90 MeV with a 2 cm thick PMMA block in front of the detector for range compensation are shown in Figure 6(b). The experimental data are compared to simulated (FLUKA^[38] Monte Carlo (MC) simulations) depth dose profiles for the respective proton beamline settings. Note that the MC simulations were benchmarked against measurements with stacks of RCF and required the implementation of a 2 MeV proton energy offset and a relative energy spread of 2.2% for the proton beam (see Figure 7 for details). In addition, the measured depth dose profiles have been corrected for the scintillator-typical light output dependence on ionization density along a proton track, in short LET (linear energy transfer)^[39]. The correction is based on the first-order model by Birks^[39], using as input the fluence-weighted LET depth distribution from the reference simulation (Figure 6(b)) and the Birks constant of $k_{BC-517H} = 0.0092 \text{ g}/(\text{MeV cm}^2)$ ^[40] for the specific scintillator material.

With these beam settings and corrections applied, the reconstructed and simulated depth dose profiles show a very good overall shape agreement and in particular an excellent agreement regarding the proton range. Only minor remaining artifacts result from the reconstruction algorithm. These artifacts concern slightly broader measured than simulated BPs. Moreover, as also observed for the 3×3 pinhole grid, the

reconstructed depth dose profiles exhibit a reduced entrance dose and wave-like structures in the plateau regions. The projections (not shown) furthermore feature an artifact in the middle of the reconstruction volume, caused by light reflection at the pinhole material. This issue may be circumvented by the choice of a different pinhole material.

In summary, the results show that multi-pinhole CB projection imaging only has a minor influence on the reconstruction result and is hence a viable option to increase detector sensitivity.

4. OCTOPOD operation at a laser-plasma accelerator proton source

4.1. Detector preparation for in-vacuum operation

Operating the OCTOPOD detector at an LPA proton source with the aim to provide online feedback on the acceleration performance is complex due to the vacuum environment in which the source is located. Since the OCTOPOD detector itself is not vacuum-compatible (e.g., liquid scintillator, silicone grease, 3D-printed material), a vacuum-compatible detector housing was designed, compact enough to be placed at less than 10 cm distance from the LPA proton source (Figure 8(a)). The vacuum housing ensures an air-pressured environment for the OCTOPOD. It has a cylindrical shape with 37 cm diameter and a length of 15 cm. The main part of the housing is made of aluminum and is closed at the rear side with a stainless steel flange. On the front plate, a 5 cm diameter opening, which is covered with a 125 μm thick Kapton foil, forms the entrance window for the proton bunch into the vacuum housing and then the OCTOPOD detector. During measurements, the Kapton window was protected by two layers of aluminum with 13 μm thickness on either side, also ensuring light tightness of the detector.

4.2. Experimental setup at Draco PW

The OCTOPOD was tested at the ultra-short pulse titanium:sapphire laser system Draco PW at HZDR, operated in a standard setting for efficient laser-driven proton acceleration in the target normal sheath acceleration (TNSA) regime^[31]. The laser pulse, containing a maximum of 18.3 J of energy after compression and plasma mirror cleaning, was focused down to a 2.6 μm full width at half maximum (FWHM) diameter spot to irradiate a 250 nm thick formvar target foil under a 50° angle of incidence.

The OCTOPOD vacuum housing was positioned at a distance of 8.5 cm behind the target foil, resulting in an effective distance of 12 cm between the LPA proton source and the sensitive volume of the OCTOPOD (Figure 8(c)). The entrance window of the detector was approximately centered on the target normal axis. To protect the detector from electrons and bremsstrahlung emitted along the laser

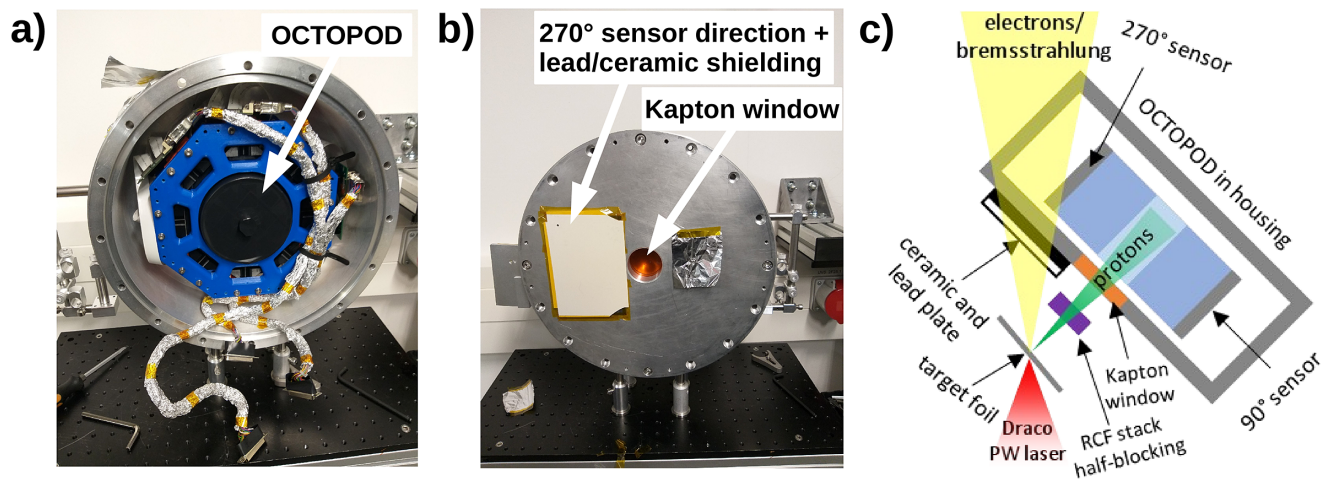


Figure 8. The setup for the OCTOPOD measurements at Draco PW. (a) Open rear side of the air-filled vacuum-compatible housing of the OCTOPOD detector. (b) Front side of the OCTOPOD housing with a thin Kapton window to enable the proton detection. The Kapton window is protected by a thin aluminum foil and the vacuum housing of the OCTOPOD detector is covered with a lead plate below a ceramic plate in laser forward direction (270°-projection sensor direction). (c) Sketch of the experimental setup at Draco PW.

axis, the front surface of the housing where the laser axis intersects was shielded with a layer of lead (Figure 8(b)).

4.3. Reference measurements against RCF and detector calibration

To reference the 3D dose distribution measured with the OCTOPOD detector and for calibration purposes, stacks of RCF (type EBT3 from Gafchromic, calibrated up to 55 Gy dose) could be positioned at a distance of 4.8 cm from the LPA proton source in front of the OCTOPOD detector using a motorized wheel. The RCF stacks were positioned such that they only partly blocked the entrance window of the OCTOPOD detector in order to enable the simultaneous measurement of the 3D proton dose distribution with both detector systems. Interlaced with copper absorbers, the first seven layers of the RCF stack sampled proton cut-off energies between 12 and 45 MeV, corresponding to a proton range in water of 1.8–18.7 mm.

For a direct comparison of 3D dose distributions measured with the OCTOPOD and an RCF stack, the dose distributions are mapped by adapting the spatial scales and accounting for the inverse-square law regarding the pixel dose. Moreover, the OCTOPOD reconstructed light distribution is transferred to dose in water by applying a density-dependent correction for the proton penetration depth and taking into account the additional stopping power for protons penetrating the OCTOPOD's front cover (aluminum protection, Kapton window, PMMA plate). All corrections applied, the OCTOPOD features a lower proton detection energy of approximately 11 MeV. In the final step, both the RCF and OCTOPOD 3D dose distribution are resampled to a voxel size of 0.5 mm, according to the reconstruction matrix of the OCTOPOD detector.

The resulting data are summarized in Figure 9, with Figure 9(a) showing the side, top and frontal (left to right) cut-plane of reconstructed 3D water dose distributions for the OCTOPOD (top) and RCF stack (bottom). As a note, the background signal in the top cut-plane (red rectangle) is a feature of the LPA process. It results from bremsstrahlung and electrons emitted in the laser forward direction, which are then detected in the 270° projection sensor located in the laser forward direction, despite additional lead shielding at this position (Figures 8(b) and 8(c)). Otherwise, both methods yield a remarkable agreement in terms of penetration depth in water (side cut-plane) and proton beam profile (frontal cut-plane). Remaining differences in the proton beam profiles are caused by a truncation of the dose scale at 55 Gy (upper dose limit of RCF calibration), which artificially homogenizes the dose distribution in the high dose region. For deeper water depths (3.5, 6, 9, 12 mm) and hence lower doses, the OCTOPOD reproduces the proton beam profile from the RCF stack reference measurement with high accuracy (Figure 9(b)). As the dose level decreases below 600 mGy (turquoise on the colormap in Figure 9(b) for water depths > 12 mm), the OCTOPOD measurements start to visibly deviate from the RCF stack reference. This indicates that the OCTOPOD is sensitive to doses down to more than or equal to 600 mGy for the reconstruction of lateral beam profiles.

For the calibration of the OCTOPOD, the proton beam profile at 3.5 mm water depth is used, yielding a calibration factor of 2.1 Gy/1 from the OCTOPOD voxel signal to the water dose.

4.4. Laser energy scan

The OCTOPOD's sensitivity to changes of the incoming proton distribution is tested by scanning the laser energy

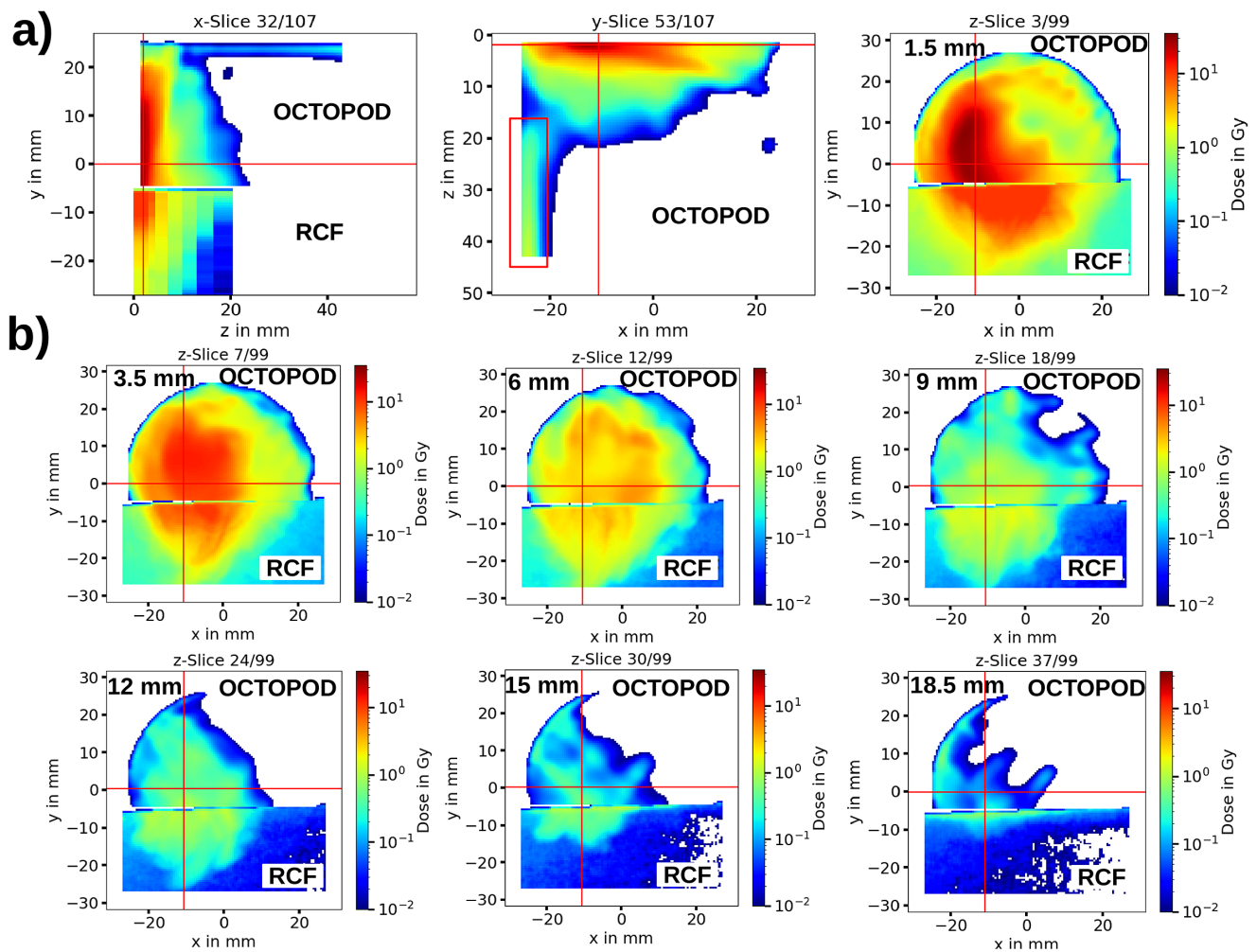


Figure 9. Comparison of cut-planes through the 3D water dose distribution measured with the OCTOPOD and a stack of radiochromic films (RCFs) as a reference detector. (a) Side, top and frontal cut-planes at 1.5 mm water depth. The red box marks a reconstruction artifact, which results from directly detected bremsstrahlung/electrons by the 270° -projection sensor. (b) Frontal cut-planes for varying water depths, as denoted in each subfigure. The red lines in each view mark the position of the other cut-planes with respect to the presented view. The signal was reconstructed with 20 iterations.

on target from 10.4 to 18.3 J in four steps. Figure 10 shows the according frontal (Figure 10(a)) and top (Figure 10(b)) cut-planes at 2.1 mm water depth derived from the reconstructed 3D water dose. The increasing penetration depth of protons into the detector as their kinetic energy increases with laser energy is clearly resolved in the depth dose distributions in Figure 10(c). From these measurements, the detection threshold is estimated to below 100 mGy because the depth dose curves feature a signal fall-off around 100 mGy that is resolved well. Note, however, that the detection threshold also depends on the overall irradiated scintillator volume versus the volume just exposed to background radiation, as this ratio affects the reconstruction performance.

The OCTOPOD's capability to record the complete proton distribution is vital here in detecting that the proton beam profile is not only increasing in diameter with increasing laser energy on target, but also shifts towards the laser forward direction ($x < 0$ mm).

4.5. Focus position scan

As a second measurement, the target position with respect to the laser pulse focus was changed for a constant laser pulse energy of 18.3 J on target (15.2 J for position $-25 \mu\text{m}$ due to saturation effects), altering the laser pulse focal spot size and hence laser intensity on target. This type of measurement constitutes a standard method to optimize the LPA proton performance, generally using the achieved proton cut-off energy as a figure of merit for optimal interaction conditions. The proton cut-off energy can be sensitive to changes in the focal spot position of less than $20 \mu\text{m}$, which is close to the achievable target alignment accuracy with respect to the focal spot position.

Figure 11 summarizes the OCTOPOD results for the frontal and top cut-planes from reconstructed 3D water doses. The TCC (target chamber center) here denotes that the target is positioned in the optically measured position of the

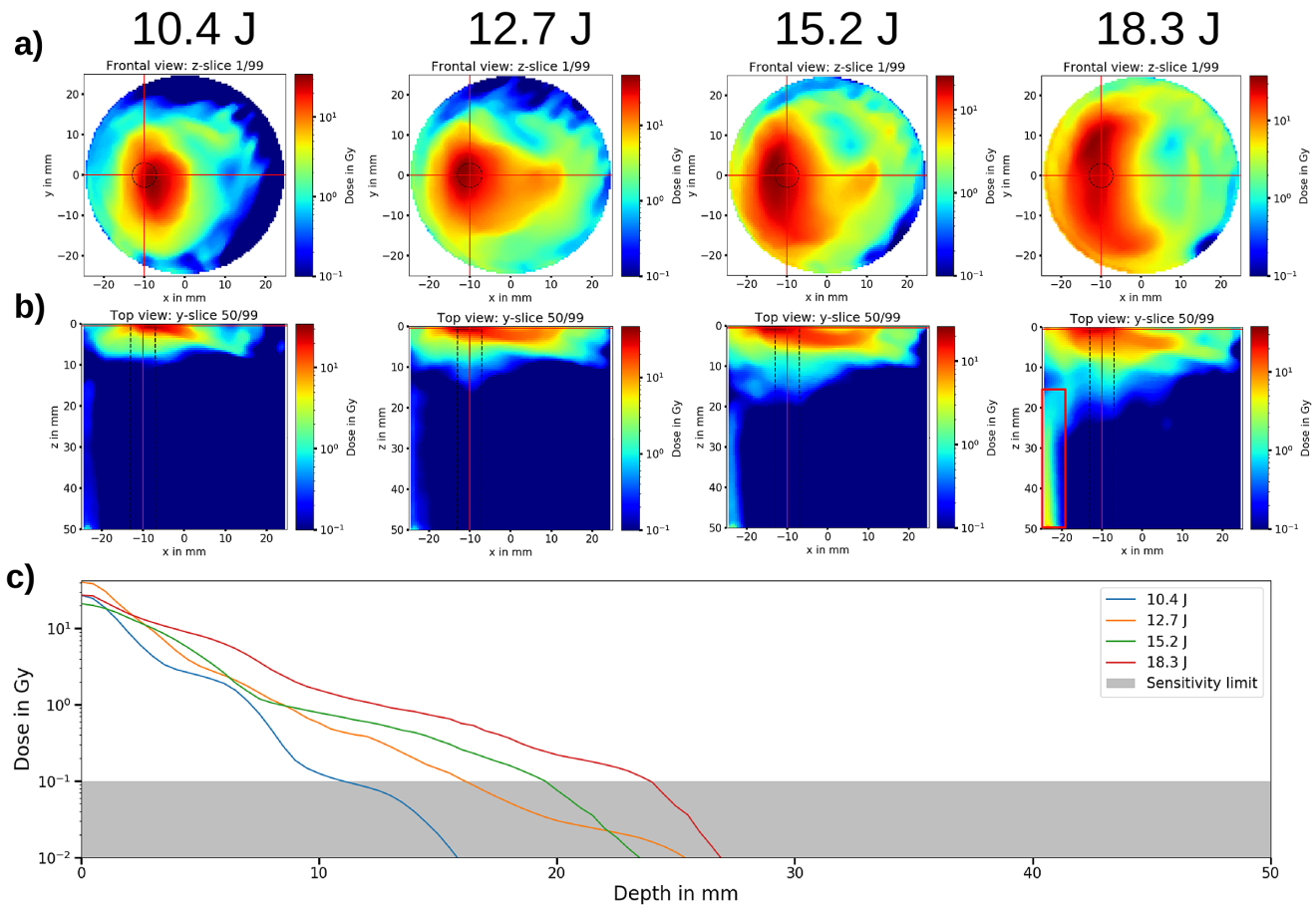


Figure 10. Influence of the laser pulse energy on the proton dose distribution. (a) Reconstructed frontal cut-planes at 2.1 mm water depth. Note that the images show the scintillator depth. (b) Reconstructed top cut-planes. (c) Mean depth dose distribution evaluated in a circular region of interest with 3 mm diameter, as marked by the black dotted circle and lines in the frontal and top cut-planes, respectively. The gray region marks where the dose sensitivity limit is estimated to be. The red lines in each view mark the position of the other cut-planes with respect to the presented view. The signal was reconstructed with 20 iterations.

laser focus and relative positions marked as positive/negative refer to target positions closer to and further away from the laser focusing optics, respectively. The top cut-planes show a clear decrease in penetration depth of the proton bunch into the detector volume with increasing distance from the TCC, in agreement with the expected decrease in proton cut-off energy with decreasing laser pulse intensity on target. As a side effect, the OCTOPOD also resolves the strong correlation between the bremsstrahlung/electron background generated in the laser forward direction (red rectangle in Figure 11) and the target position, that is, the laser pulse intensity on target.

Whereas these features may also be detected with alternative methods, for example, Thomson parabola/bremsstrahlung/electron spectrometers, the OCTOPOD provides the full proton beam profiles, here at a water depth of 2.1 mm reachable by protons with kinetic energies exceeding 13.5 MeV. Around the TCC ($\pm 25 \mu\text{m}$), the proton beam profile is shifted towards the laser forward direction ($x < 0 \text{ mm}$), as observed for the laser energy scan, and shifts back into the direction of the target normal direction further

away from TCC. For positions where $\text{TCC} > +50 \mu\text{m}$, the OCTOPOD resolves a rotation of the proton beam profile and a double peak structure for $\text{TCC} = +50 \mu\text{m}$. This behavior can be indicative of hybrid acceleration schemes^[41], but may also be related to spatio-temporal coupling effects in the laser focus imprinting into the proton beam profile^[6].

5. Discussion and summary

To conclude, the OCTOPOD detector is a solution to the long-standing challenge in detecting the full angular-spectral distribution of single LPA proton bunches in real-time. Careful choice of the projection approach (pinhole imaging) and light guiding design makes the detector compact enough to be placed close to the laser–target interaction region. Performing systematic characterization measurements at a cyclotron proton source, we could show the OCTOPOD’s capabilities in reliably reconstructing 3D dose distributions with mm-scale spatial resolution. Operated at the LPA proton source, the OCTOPOD was shown to be sensitive to minimal

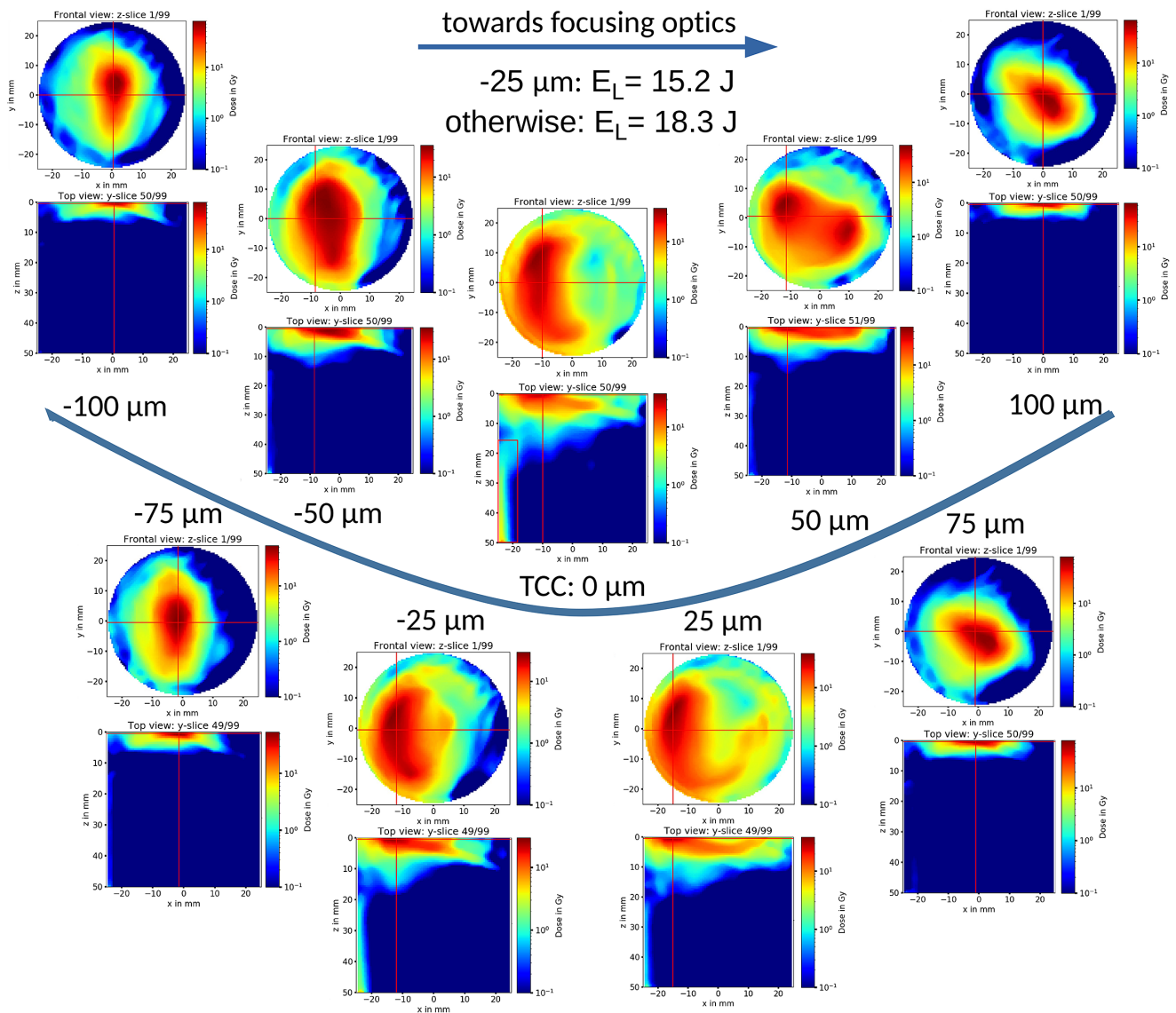


Figure 11. Scan of the focal spot position on target showing the top and frontal cut-planes at 2.1 mm water depth (≥ 13.5 MeV proton energy) of the 3D water dose distribution measured with the OCTOPOD. The blue curved line represents the focus size. The target chamber center (TCC) is at $0 \mu\text{m}$ and the positive target position changes are in the direction of the focusing optics. The laser energy on target is $E_L = 18.3$ J, except for the target position $-25 \mu\text{m}$ ($E_L = 15.2$ J). The red lines in each view mark the position of the other cut-planes with respect to the presented view. The signal was reconstructed with 20 iterations.

changes in the laser–target interaction conditions, for example, changes in the focal spot position of $25 \mu\text{m}$.

A further miniaturization of the setup and hence wider dissemination can be achieved by replacing the liquid scintillator with a plastic scintillator block and when using vacuum-compatible components throughout the detector design (e.g., silicone grease for the immersion of interfaces). In that case, the requirement for the bulky vacuum-compatible detector housing would be lifted. The housing has proven to allow for stable detector operation in the harsh plasma environment (optical and particle emission from the plasma emission, electromagnetic pulses) at a PW-class high-power laser system. However, the RadEye sensors can

also be operated directly in vacuum when shielded from background radiation.

For any practical purpose, the OCTOPOD needs to be competitive with the established and hence trusted LPA proton detector systems Thomson parabola and RCF. In comparison to RCF, the OCTOPOD features a similar lower detection threshold of 100 mGy, providing comparable proton cut-off energy detectability. Moreover, the OCTOPOD can be operated with various pinhole configurations, also in combination for different projection directions. This feature gives a handle on the detector’s dynamic range and can prevent signal saturation for the low-energy portion of the spectrum, a general issue with RCF. The spectral resolution

of the OCTOPOD is influenced by the detector's spatial resolution, which is a factor of 4 higher for RCF (280 μm thickness) than for the OCTOPOD (1 mm theoretical spatial resolution). Note that the given spatial resolution for the OCTOPOD is theoretical, not taking into account the influence of, for example, scintillation light scattering inside the scintillator volume. Yet, for most practical purposes of detecting protons with kinetic energies in the multi-10 MeV range, RCF will be interlaced with absorbers in a stack setup. This limits the effective energy resolution to below the OCTOPOD's capabilities and additionally introduces the uncertainty of signal generation in the RCF from proton-triggered nuclear reactions in the absorber material.

For TPs, the spectral resolution and cut-off energy detectability, particularly when operated with micro-channel plate detectors, are clearly higher than for the OCTOPOD detector, but the reduced angular acceptance introduces the uncertainty of whether the highest energy protons of a bunch are detected at all.

In summary, the unique capability of the OCTOPOD detector is the single pulse real-time detection of the full angular-spectral proton distribution with a sensitivity, dynamic range and spatial resolution adapted to the needs of current proton LPA experiments. A number of application scenarios will profit from this detector type. Firstly, the capability of a full characterization of the proton bunch will provide considerably better and most importantly statistical input data for LPA proton beamlines^[42] and hence further promote the development of application experiments and the according instrumentation. Moreover, the OCTOPOD can enable an automated feedback loop between laser parameters governing the complex plasma dynamics of the acceleration process and a targeted application-specific 3D angular-spectral distribution. For both LPA electrons and protons, such automated feedback loops have successfully been implemented recently^[43,44]. The OCTOPOD will also open up new possibilities in investigating the spatio-temporal coupling effect in the laser pulse^[45] affecting acceleration performance and angular proton emission patterns. Last but not least, a dedicated investigation of the spatial resolution limits as also affected by pinhole arrays might qualify the OCTOPOD as a viable detector for proton radiography studies^[46].

Acknowledgements

We gratefully acknowledge the DRACO laser team and UPTD team for excellent experiment support. The work was partially supported by H2020 Laserlab Europe V (PRISES, contract No. 871124) and by the European Union's Horizon 2020 Research and Innovation Programme Impulse (grant agreement No. 871161). We recognize the support of the Weizmann-Helmholtz Laboratory for Laser Matter Interaction (WHELMI). The experimental part of the University Proton Therapy Dresden (UPTD) facility has

received funding from the European Union's Horizon 2020 Research and Innovation Program (grant agreement No. 730983 (INSPIRE)).

References

1. F. Albert, M. E. Couprie, A. Debus, M. C. Downer, J. Faure, A. Flacco, L. A. Gizzi, T. Grismayer, A. Huebl, C. Joshi, M. Labat, W. P. Leemans, A. R. Maier, S. P. Mangles, P. Mason, F. Mathieu, P. Muggli, M. Nishiuchi, J. Osterhoff, P. P. Rajeev, U. Schramm, J. Schreiber, A. G. Thomas, J. L. Vay, M. Vranic, and K. Zeil, *New J. Phys.* **23**, 031101 (2021).
2. F. Kroll, F.-E. Brack, C. Bernert, S. Bock, E. Bodenstern, K. Brüchner, T. E. Cowan, L. Gaus, R. Gebhardt, U. Helbig, L. Karsch, T. Kluge, S. Kraft, M. Krause, E. Lessmann, U. Masood, S. Meister, J. Metzkes-Ng, A. Nossula, J. Pawelke, J. Pietzsch, T. Püschel, M. Reimold, M. Rehwald, C. Richter, H.-P. Schlenvoigt, U. Schramm, M. E. P. Umlandt, T. Ziegler, K. Zeil, and E. Beyreuther, *Nat. Phys.* **18**, 316 (2022).
3. P. Chaudhary, G. Milluzzo, H. Ahmed, B. Odlozilik, A. McMurray, K. M. Prise, and M. Borghesi, *Front. Phys.* **9**, 1 (2021).
4. M. Barberio, S. Veltri, M. Scisciò, and P. Antici, *Sci. Rep.* **7**, 40415 (2017).
5. P. Sommer, J. Metzkes-Ng, F.-E. Brack, T. E. Cowan, S. D. Kraft, L. Obst, M. Rehwald, H.-P. Schlenvoigt, U. Schramm, and K. Zeil, *Plasma Phys. Control. Fusion* **60**, 054002 (2018).
6. K. Zeil, J. Metzkes, T. Kluge, M. Bussmann, T. E. Cowan, S. D. Kraft, R. Sauerbrey, and U. Schramm, *Nat. Commun.* **3**, 874 (2012).
7. K. Harres, M. Schollmeier, E. Brambrink, P. Audebert, A. Blažević, K. Flippo, D. C. Gautier, M. Geißel, B. M. Hegelich, F. Nürnberg, J. Schreiber, H. Wahl, and M. Roth, *Rev. Sci. Instrum.* **79**, 093306 (2008).
8. D. C. Carroll, P. Brummitt, D. Neely, F. Lindau, O. Lundh, C. G. Wahlström, and P. McKenna, *Nucl. Instrum. Methods Phys. Res. Sect. A* **620**, 23 (2010).
9. D. Jung, R. Hrlein, D. Kiefer, S. Letzring, D. C. Gautier, U. Schramm, C. Hbsch, R. Hm, B. J. Albright, J. C. Fernandez, D. Habs, and B. M. Hegelich, *Rev. Sci. Instrum.* **82**, 013306 (2011).
10. P. R. Bolton, M. Borghesi, C. Brenner, D. C. Carroll, C. De Martinis, F. Fiorini, A. Flacco, V. Floquet, J. Fuchs, P. Gallegos, D. Giove, J. S. Green, S. Green, B. Jones, D. Kirby, P. McKenna, D. Neely, F. Nuesslin, R. Prasad, S. Reinhardt, M. Roth, U. Schramm, G. G. Scott, S. Ter-Avetisyan, M. Tolley, G. Turchetti, and J. J. Wilkens, *Phys. Med.* **30**, 255 (2014).
11. M. Würfl, F. S. Englbrecht, S. Lehrack, C. Gianoli, F. H. Lindner, T. F. Rösch, D. Haffa, F. Olivari, M. Petasecca, M. L. Lerch, A. Pogosso, L. T. Tran, W. Assmann, J. Schreiber, A. B. Rosenfeld, and K. Parodi, *Rev. Sci. Instrum.* **89**, 123302 (2018).
12. G. Milluzzo, V. Scuderi, A. Alejo, A. G. Amico, N. Booth, M. Borghesi, G. A. Cirrone, G. Cuttone, D. Doria, J. Green, S. Kar, G. Korn, G. Larosa, R. Leanza, D. Margarone, P. Martin, P. McKenna, G. Petringa, J. Pipek, L. Romagnani, F. Romano, A. Russo, and F. Schillaci, *Rev. Sci. Instrum.* **90**, 083303 (2019).
13. M. Salvadori, F. Consoli, C. Verona, M. Cipriani, M. P. Anania, P. L. Andreoli, P. Antici, F. Bisesto, G. Costa, G. Cristofari, R. De Angelis, G. Di Giorgio, M. Ferrario, M. Galletti, D. Giulietti, M. Migliorati, R. Pompili, and A. Zigler, *Sci. Rep.* **11**, 3071 (2021).
14. M. Reimold, S. Assenbaum, C. Bernert, E. Beyreuther, F.-E. Brack, L. Karsch, S. Kraft, F. Kroll, M. Loeser, A. Nossula, J. Pawelke, T. Püschel, H.-P. Schlenvoigt, U. Schramm,

- M. Umlandt, K. Zeil, T. Ziegler, and J. Metzkes-Ng, *Sci. Rep.* **12**, 21488 (2022).
15. F. Nürnberg, M. Schollmeier, E. Brambrink, A. Blažević, D. C. Carroll, K. Flippo, D. C. Gautier, M. Geibel, K. Harres, B. M. Hegelich, O. Lundh, K. Markey, P. McKenna, D. Neely, J. Schreiber, and M. Roth, *Rev. Sci. Instrum.* **80**, 033301 (2009).
 16. J. S. Green, M. Borghesi, C. M. Brenner, D. C. Carroll, N. P. Dover, P. S. Foster, P. Gallegos, S. Green, D. Kirby, K. J. Kirkby, P. McKenna, M. J. Merchant, Z. Najmudin, C. A. J. Palmer, D. Parker, R. Prasad, K. E. Quinn, P. P. Rajeev, M. P. Read, L. Romagnani, J. Schreiber, M. J. V. Streeter, O. Tresca, C.-G. Wahlström, M. Zepf, and D. Neely, *Proc. SPIE* **8079**, 807919 (2011).
 17. J. Metzkes, L. Karsch, S. D. Kraft, J. Pawelke, C. Richter, M. Schürer, M. Sobiella, N. Stiller, K. Zeil, and U. Schramm, *Rev. Sci. Instrum.* **83**, 123301 (2012).
 18. J. Metzkes, K. Zeil, S. D. Kraft, L. Karsch, M. Sobiella, M. Rehwald, L. Obst, H. P. Schlenvoigt, and U. Schramm, *Rev. Sci. Instrum.* **87**, 083310 (2016).
 19. N. P. Dover, M. Nishiuchi, H. Sakaki, M. A. Alkhimova, A. Y. Faenov, Y. Fukuda, H. Kiriyaama, A. Kon, K. Kondo, K. Nishitani, K. Ogura, T. A. Pikuz, A. S. Pirozhkov, A. Sagisaka, M. Kando, and K. Kondo, *Rev. Sci. Instrum.* **88**, 073304 (2017).
 20. M. Huault, D. De Luis, J. I. Apiñaniz, M. De Marco, C. Salgado, N. Gordillo, C. Gutiérrez Neira, J. A. Pérez-Hernández, R. Fedosejevs, G. Gatti, L. Roso, and L. Volpe, *High Power Laser Sci. Eng.* **7**, e60 (2019).
 21. K. M. Schwind, E. Aktan, R. Prasad, M. Cerchez, D. Eversheim, O. Willi, and B. Aurand, *Rev. Sci. Instrum.* **90**, 053307 (2019).
 22. M. J.-E. Manuel, H. Tang, B. K. Russell, L. Willingale, A. Maksimchuk, J. S. Green, E. L. Alfonso, J. Jaquez, L. Carlson, D. Neely, and T. Ma, *Rev. Sci. Instrum.* **91**, 103301 (2020).
 23. M. Hesse, T. Ebert, M. Zimmer, S. Scheuren, and M. Roth, *Rev. Sci. Instrum.* **92**, 093302 (2021).
 24. D. A. Mariscal, B. Z. Djordjević, E. S. Grace, R. Hollinger, T. Ma, G. G. Scott, H. Song, R. A. Simpson, J. J. Rocca, and S. Wang, *Plasma Phys. Control. Fusion* **63**, 114003 (2021).
 25. D. Haffa, R. Yang, J. Bin, S. Lehrack, F. E. Brack, H. Ding, F. S. Englbrecht, Y. Gao, J. Gebhard, M. Gilljohann, J. Götzfried, J. Hartmann, S. Herr, P. Hilz, S. D. Kraft, C. Kreuzer, F. Kroll, F. H. Lindner, J. Metzkes-Ng, T. M. Ostermayr, E. Ridente, T. F. Rösch, G. Schilling, H. P. Schlenvoigt, M. Speicher, D. Taray, M. Würfl, K. Zeil, U. Schramm, S. Karsch, K. Parodi, P. R. Bolton, W. Assmann, and J. Schreiber, *Sci. Rep.* **9**, 6714 (2019).
 26. S. Gerlach, F. Balling, A. K. Schmidt, F. E. Brack, F. Kroll, M. Reimold, U. Schramm, M. Speicher, K. Zeil, K. Parodi, and J. Schreiber, *High Power Laser Sci. Eng.* **11**, e38 (2023).
 27. L. Archambault, F. Poenisch, N. Sahoo, D. Robertson, A. Lee, M. T. Gillin, R. Mohan, and S. Beddar, *Med. Phys.* **39**, 1239 (2012).
 28. N. U. Schramm, G. Ebel, U. Engeland, T. Schurrat, M. Béhé, and T. M. Behr, *IEEE Nucl. Sci. Symp. Med. Imag. Conf.* **2**, 774 (2002).
 29. B. Schmitz, M. Metternich, and O. Boine-Frankenheim, *Rev. Sci. Instrum.* **93**, 093306 (2022).
 30. U. Schramm, M. Bussmann, A. Irman, M. Siebold, K. Zeil, D. Albach, C. Bernert, S. Bock, F. Brack, J. Branco, J. P. Couperus, T. E. Cowan, A. Debus, C. Eisenmann, M. Garten, R. Gebhardt, S. Grams, U. Helbig, A. Huebl, T. Kluge, A. Köhler, J. M. Krämer, S. Kraft, F. Kroll, M. Kuntzsch, U. Lehnert, M. Loeser, J. Metzkes, P. Michel, L. Obst, R. Pausch, M. Rehwald, R. Sauerbrey, H. P. Schlenvoigt, K. Steiniger, and O. Zarini, *J. Phys. Conf. Ser.* **874**, 012028 (2017).
 31. T. Ziegler, D. Albach, C. Bernert, S. Bock, F. E. Brack, T. E. Cowan, N. P. Dover, M. Garten, L. Gaus, R. Gebhardt, I. Goethel, U. Helbig, A. Irman, H. Kiriyaama, T. Kluge, A. Kon, S. Kraft, F. Kroll, M. Loeser, J. Metzkes-Ng, M. Nishiuchi, L. Obst-Huebl, T. Püschel, M. Rehwald, H. P. Schlenvoigt, U. Schramm, and K. Zeil, *Sci. Rep.* **11**, 7338 (2021).
 32. S. Reinhardt, W. Draxinger, J. Schreiber, and W. Assmann, *J. Instrum.* **8**, P03008 (2013).
 33. F. S. Englbrecht, M. Würfl, F. Olivari, A. Ficarella, C. Kreuzer, F. H. Lindner, M. D. Palma, L. Pancheri, G.-F. D. Betta, J. Schreiber, A. Quaranta, and K. Parodi, *Radiat. Protect. Dosimetry* **180**, 291 (2018).
 34. F. H. Lindner, J. H. Bin, F. Englbrecht, D. Haffa, P. R. Bolton, Y. Gao, J. Hartmann, P. Hilz, C. Kreuzer, T. M. Ostermayr, T. F. Rösch, M. Speicher, K. Parodi, P. G. Thirolf, and J. Schreiber, *Rev. Sci. Instrum.* **89**, 013301 (2018).
 35. M. Bertero, and P. Boccacci, *A&A* **437**, 369 (2005).
 36. S. Helmbrecht, M. Baumann, W. Enghardt, F. Fiedler, M. Krause, and A. Lühr, *J. Instrum.* **11**, T11001 (2016).
 37. S. E. Anderson, M. P. Grams, H. W. C. Tseung, K. M. Furutani, and C. J. Beltran, *Phys. Med. Biol.* **64**, 055015 (2019).
 38. G. Battistoni, J. Bauer, T. T. Boehlen, F. Cerutti, M. P. Chin, R. Dos Santos Augusto, A. Ferrari, P. G. Ortega, W. Kozłowska, G. Magro, A. Mairani, K. Parodi, P. R. Sala, P. Schoofs, T. Tessonnier, and V. Vlachoudis, *Front. Oncol.* **6**, 116 (2016).
 39. J. Birks, *The Theory and Practice of Scintillation Counting*, International Series of Monographs in Electronics and Instrumentation (Pergamon Press, 1964).
 40. B. Braizinha, J. H. Esterline, H. J. Karwowski, and W. Tornow, *Nucl. Instrum. Methods Phys. Res. Sect. A* **623**, 1046 (2010).
 41. A. Higginson, R. J. Gray, M. King, R. J. Dance, S. D. Williamson, N. M. Butler, R. Wilson, R. Capdessus, C. Armstrong, J. S. Green, S. J. Hawkes, P. Martin, W. Q. Wei, S. R. Mirfayzi, X. H. Yuan, S. Kar, M. Borghesi, R. J. Clarke, D. Neely, and P. McKenna, *Nat. Commun.* **9**, 724 (2018).
 42. F. E. Brack, F. Kroll, L. Gaus, C. Bernert, E. Beyreuther, T. E. Cowan, L. Karsch, S. Kraft, L. A. Kunz-Schughart, E. Lessmann, J. Metzkes-Ng, L. Obst-Huebl, J. Pawelke, M. Rehwald, H. P. Schlenvoigt, U. Schramm, M. Sobiella, E. R. Szabó, T. Ziegler, and K. Zeil, *Sci. Rep.* **10**, 9118 (2020).
 43. S. Jalas, M. Kirchen, P. Messner, P. Winkler, L. Hübner, J. Dirkwinkel, M. Schnepp, R. Lehe, and A. R. Maier, *Phys. Rev. Lett.* **126**, 104801 (2021).
 44. B. Loughran, M. J. V. Streeter, H. Ahmed, S. Astbury, M. Balcazar, M. Borghesi, N. Bourgeois, C. B. Curry, S. J. D. Dann, S. DiIorio, N. P. Dover, T. Dzelzanis, O. C. Ettlinger, M. Gauthier, L. Giuffrida, G. D. Glenn, S. H. Glenzer, J. S. Green, R. J. Gray, G. S. Hicks, C. Hyland, V. Istokskaia, M. King, D. Margarone, O. McCusker, P. McKenna, Z. Najmudin, C. Parisuaña, P. Parsons, C. Spindloe, D. R. Symes, A. G. R. Thomas, F. Treffert, N. Xu, and C. A. J. Palmer, *High Power Laser Sci. Eng.* **11**, e35 (2023).
 45. A. Jeandet, S. W. Jolly, A. Borot, B. Bussière, P. Dumont, J. Gautier, O. Gobert, J.-P. Goddet, A. Gonsalves, A. Irman, W. P. Leemans, R. Lopez-Martens, G. Menerat, K. Nakamura, M. Ouilé, G. Pariente, M. Pittman, T. Püschel, F. Sanson, F. Sylla, C. Thauray, K. Zeil, and F. Quéré, *Opt. Express* **30**, 3262 (2022).
 46. L. Romagnani, J. Fuchs, M. Borghesi, P. Antici, P. Audebert, F. Ceccherini, T. Cowan, T. Grismayer, S. Kar, A. Macchi, P. Mora, G. Pretzler, A. Schiavi, T. Toncian, and O. Willi, *Phys. Rev. Lett.* **95**, 195001 (2005).